Jurnal Teknik Sipil
p-ISSN 2088-9321
e-ISSN 2502-5295
Volume 13 No. 1, Mei 2024

NUMERICAL ANALYSIS OF STEEL MEMBER REMAINING COMPRESSIVE CAPACITY DURING SHIELDED METAL ARC WELDING

Malik Mushthofa[1*], Astriana Hardawati[2]
[1,2)] Islamic University of Indonesia, Indonesia
Kaliurang St No.Km. 14,5, Ngemplak, Sleman Regency, Special Region of Yogyakarta 55584

[*)]email: malik.mushthofa@uii.ac.id

Diterima : 22 April 2024
Direvisi : 15 May 2024
Disetujui : 16 May 2024
Diterbitkan : 31 May 2024

Abstract: *This study investigates the influence of Shielded Metal Arc Welding (SMAW) welding parameters on the remaining compressive capacity of angle-shaped steel members used for structural strengthening. The analysis focuses on members with thin hot-rolled profiles (40.4 x 40.4 x 4.0 mm, 50.5 x 50.5 x 5.0 mm, and 60.6 x 60.6 x 6.0 mm). A finite element model simulates the heat distribution caused by welding, leading to a temperature increase within the member. Welding scenarios are simulated using various combinations of current strength and welding speed based on the specifications for electrode type E6013. The remaining compressive capacity is determined by segmenting the cross-section based on temperature intervals and considering the member's slenderness. The analysis reveals a clear correlation between welding parameters and compressive capacity loss. Employing a higher current and lower welding speed leads to a more significant reduction in capacity due to the resulting extensive heat-affected zone (HAZ). Conversely, the lowest current and highest speed scenario minimizes the HAZ, resulting in the highest remaining compressive capacity. The analysis demonstrates that the 40.4 x 40.4 x 4.0 mm member can retain up to 51.15% of its original capacity under these optimal conditions, while the 50.5 x 50.5 x 5.0 mm and 60.6 x 60.6 x 6.0 mm members can retain 57.79% and 75.78%, respectively. In contrast, the worst-case scenario employing high current and low speed significantly reduces the remaining capacity, with reductions down to 6.79%, 10.87%, and 10.54% for the respective member sizes. These findings highlight the importance of optimizing welding parameters to minimize the negative impact on the compressive capacity of steel members during strengthening operations.*

Keywords : *compressive capacity, current, heat, SMAW welding, welding speed*

1. INTRODUCTION

The growing need for infrastructure retrofitting emphasizes the importance of adapting existing structures to enhance serviceability [1]. Over time, changes in population demographics, technological advancements, and evolving regulations can render infrastructure inadequate [2]. Addressing serviceability improvements in operational infrastructure often requires interventions while the structure remains under service load [3]. This critical aspect underscores the necessity for meticulous planning and precise execution to minimize disruptions during the retrofitting process, especially in steel-made construction.

Within critical infrastructure systems, specific components are irreplaceable and must maintain continuous operation. Hospitals and their supporting utilities, such as water reservoirs, exemplify this principle [2]. The uninterrupted functionality of these elements underscores their vital role in upholding essential services [4]. Steel, reinforced concrete, and timber are common construction materials that form the backbone of our built environment. However, steel structures present a distinct challenge when it comes to retrofitting due to the inherent heat involved in the welding process [5, 6]. Welding, a cornerstone of structural modifications, can negatively impact the integrity of steel members through heat generation [7]. While bolted and welded joints offer options for connecting steel members, it's noteworthy that both methods incorporate some form of welding [8].

Truss structures, characterized by their intricate network of slender members, exhibit a greater susceptibility to heat-related effects compared to frame

structures [9]. This distinction stems from the inherent design principles of trusses, which often incorporate members with smaller cross-sectional areas [10]. In contrast to frame structures that typically utilize larger, more robust elements, trusses rely on the combined strength of their interconnected members to achieve their structural function [11]. As a consequence, any reduction in the structural integrity of these slender members, such as that caused by heat exposure, can significantly impact the overall stability and performance of the entire truss system [12].

Research by Mushthofa [13] has established a critical correlation between the thickness of steel sections and the dimensions of the heat-affected zone (HAZ) during welding. This finding highlights a key aspect of the welding process: the material's thickness directly influences the extent of thermal alteration in its surrounding area [14]. When welding thinner steel sections, the generated heat penetrates a larger portion of the material, resulting in a wider HAZ compared to thicker sections [15].

Truss structures are well-known for their efficient ability to transmit axial stresses, encompassing both compression and tension, within their members [16]. However, it is crucial to recognize that the compressive capacity of these members is not solely determined by the material's strength but also by their geometric properties, particularly their length. This relationship is captured by the slenderness parameter, which represents the ratio of a member's length to its cross-sectional dimensions [17]. In trusses, where members are slender and primarily subjected to axial loads, the capacity to resist compressive stress exhibits a non-linear dependence on member length [18]. As the ratio of member length to cross-sectional dimensions increases, susceptibility to buckling increases, thereby compromising their effectiveness in resisting compressive forces [18].

Previous research has predominantly focused on evaluating the strength and integrity of welded joints [19] or examining their properties after the welding process [20]. However, a significant knowledge gap persists regarding the behavior of welded members under load, especially at elevated temperatures encountered during fire events [21]. While existing studies have explored the behavior of structural elements under fire conditions, the emphasis is often placed on the overall structural response rather than the specific behavior of the welded members themselves [22]. This study aims to address this critical gap by investigating the capacity of welded members subjected to combined loading and elevated temperature conditions.

This paper presents the results of an analysis investigating the effects of welding on the compressive capacity of steel members. The analysis explores the influence of three key parameters: steel member thickness, welding speed, and electrical current used on the electrode. The impact of these parameters on the remaining compressive capacity is evaluated for steel members of varying lengths.

2. THEORY AND METHODS

Theory

The Heat Affected Zone (HAZ) is a crucial region surrounding the molten weld pool in a welded joint. While the weld pool itself undergoes complete melting, the HAZ experiences significant temperature elevations during the welding process. This localized heating induces metallurgical transformations in the base metal without complete melting. These transformations alter the microstructure and mechanical properties of the material [21]. Consequently, the HAZ can exhibit reduced strength and ductility, increased hardness and brittleness, and a heightened susceptibility to cracking compared to the unaffected base metal [22]. Higher heat input during the welding process results in a larger and more pronounced HAZ. Material properties also play a significant role, with thinner materials generally exhibiting wider HAZ compared to thicker sections due to differences in thermal conductivity.

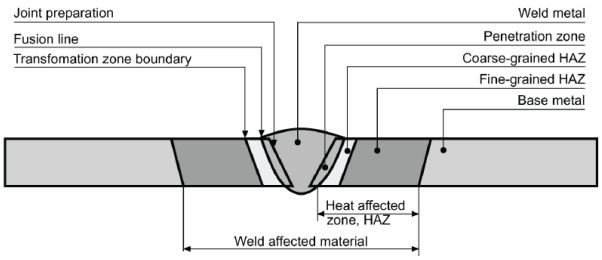

Figure 1. Heat affected zone division during welding [23]

A cross-section of a welded joint can be conceptually divided into two distinct regions: the heat-affected zone (HAZ) and the base metal (**Figure 1**). The capacity of a member to resist compressive forces, known as its compressive strength, transcends the intrinsic properties of the material itself. It is a complex interaction governed by several key parameters [24]. The effective length factor (k) reflects the support conditions of the member. A more rigid support system (higher k) translates to a higher attainable compressive strength [25]. The member length (L) exerts a straightforward influence: longer members exhibit a greater susceptibility to buckling under compression due to the amplified leverage for bending moments [26]. The radius of gyration (r) plays a crucial role, as it relates to the distribution of the member's area (A) and moment of inertia (I) [27]. A larger radius of gyration signifies a stockier member with enhanced resistance to buckling,

thereby leading to a higher compressive strength. Finally, the material's yield strength (fy) also comes into play. A material with a higher yield strength can withstand a greater compressive load before yielding and potentially buckling. It's important to note that these parameters are not independent; for instance, the effective length factor can influence the critical buckling load, which itself depends on the member's length and radius of gyration.

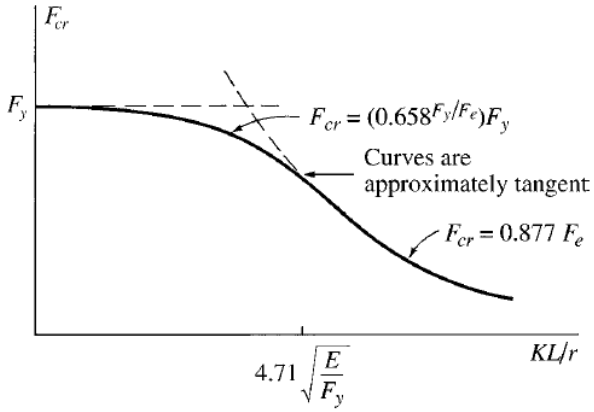

Figure 2. Elastic and in-elastic limit columns [27]

The design of structures incorporating compression members, such as columns, necessitates a thorough understanding of their behavior under load. Columns can be classified as either elastic or inelastic (**Figure 2**) based on their response to compressive forces. Elastic columns are perfectly straight, slender members fabricated from a material with well-defined yield strength (Fy) and elastic modulus (E). These columns exhibit a specific response when subjected to gradually increasing compressive loads. Initially, the column undergoes elastic deformation that is proportional to the applied load. This initial behavior follows a well-defined linear relationship between stress and strain, as governed by Hooke's Law. However, a critical load limit exists, beyond which the column can experience lateral buckling. Euler's formula provides an estimate for this critical buckling load in elastic columns. It incorporates the column length (L), the material's elastic modulus (E), and a factor (k) that reflects the end conditions of the column.

Inelastic columns, characterized by stockier cross-sections or fabrication from materials with lower yield strengths (Fy), exhibit behavior that deviates from the purely elastic regime. In these cases, the column transitions into the inelastic region, where the stress-strain relationship becomes nonlinear. This nonlinearity signifies material yielding, which can induce permanent deformation even before the critical buckling load is reached. Consequently, the critical load capacity for inelastic columns is generally lower than that predicted by Euler's formula for elastic columns. To account for the influence of material properties and geometry on buckling behavior, empirical formulas can be employed. One such formula estimates the critical load for inelastic columns using a constant (4.71) multiplied by the square root of the ratio between the elastic modulus (E) and yield strength (Fy). This emphasizes the critical importance of considering both the material properties and geometric factors when designing columns for adequate resistance to buckling under compressive loads.

Methods

The numerical analysis is conducted on the thinnest commercially available hot-rolled angle sections commonly used in structural applications. These sections have the following dimensions: L 40.40.4, L 50.50.5, and L 60.60.6 (where L represents the equal leg length). Shielded Metal Arc Welding (SMAW) is employed, utilizing the E6013 electrode, a popular choice for general-purpose welding [28].

According to ASME Section IX [29], the following equation (1) is used for calculating heat input:

$$HI = (V\,.\,A\,.60\,)/s \qquad (1)$$

where HI is heat input (kJ/mm), V is voltage (V), A is current (Amps), and s is welding speed (mm/min). EN ISO 1011-1 [30] gives the thermal efficiency value for SMAW as 0.8. These variations will produce different energy input (Hnet) values, as shown in **Table 1** below. The simulation was conducted using a 3.2 mm diameter electrode with a static voltage of 35 V. The travel speed varied from 75 mm/min to 150 mm/min in increments of 10 mm/min. The current was varied across multiple simulations, ranging from 75 amps to 125 amps with 10 amp intervals.

The electrode diameter and current values are referenced in the product catalog. A constant voltage of 35 V is employed in this study. This value represents the upper limit typically recommended for SMAW processes. The decision to maintain a constant voltage stems from the understanding that, in SMAW, electrode diameter exerts a greater influence on current and penetration depth compared to voltage [31]. Increasing voltage beyond the recommended range is not expected to yield significant benefits.

The selection of travel speeds draws reference from several studies and industry catalogs ([32], [33], [34]). These resources recommend a travel speed range of 3 to 6 inches per minute (75–150 mm/min) for SMAW welding processes.

Thermal efficiency in welding refers to the portion of electrical energy supplied to the arc that translates into heating the weld pool. A nominal value of 0.8 is often assumed, but several factors influence the effectiveness of this energy transfer [35].

A key factor is the inherent variability of the heat source in Shielded Metal Arc Welding (SMAW) compared to more focused processes [35]. SMAW relies on resistance heating of the electrode tip and molten metal droplet, resulting in less-controlled heat input and potential fluctuations in the amount of heat transferred to the workpiece [36]. Travel speed and electrode size also play a role. Higher travel speeds or larger electrode diameters limit the time available for the arc to heat the metal, leading to lower thermal efficiency. Material properties further influence efficiency. Materials with higher thermal conductivity dissipate heat more readily, reducing the energy available to heat the weld pool. Finally, while machine settings have a minor influence, higher voltage settings can lead to a slight decrease in efficiency due to increased arc length, but this effect is generally less significant compared to the other factors [37]. As Kah [38] highlighted, arc efficiency varies depending on factors such as arc voltage and current. Their research does not provide a single definitive value for SMAW, but emphasizes the importance of considering these parameters to achieve optimal welding outcomes.

Table 1. Energy input and simulation mapping

Scenario Num. for 75 Amps	**S 1.1**	**S 1.2**	**S 1.3**	**S 1.4**	**S 1.5**	**S 1.6**	**S 1.7**	**S 1.8**
Travel speed (mm/min)	75	85	95	105	115	125	135	150
Energy input (kJ/mm)	1.680	1.482	1.326	1.200	1.096	1.008	0.933	0.840
Scenario Num. for 85 Amps	**S 2.1**	**S 2.2**	**S 2.3**	**S 2.4**	**S 2.5**	**S 2.6**	**S 2.7**	**S 2.8**
Travel speed (mm/min)	75	85	95	105	115	125	135	150
Energy input (kJ/mm)	1.904	1.680	1.503	1.360	1.242	1.142	1.058	0.952
Scenario Num. for 95 Amps	**S 3.1**	**S 3.2**	**S 3.3**	**S 3.4**	**S 3.5**	**S 3.6**	**S 3.7**	**S 3.8**
Travel speed (mm/min)	75	85	95	105	115	125	135	150
Energy input (kJ/mm)	2.128	1.878	1.680	1.520	1.388	1.277	1.182	1.064
Scenario Num. for 105 Amps	**S 4.1**	**S 4.2**	**S 4.3**	**S 4.4**	**S 4.5**	**S 4.6**	**S 4.7**	**S 4.8**
Travel speed (mm/min)	75	85	95	105	115	125	135	150
Energy input (kJ/mm)	2.352	2.075	1.875	1.680	1.534	1.411	1.307	1.176
Scenario Num. for 115 Amps	**S 5.1**	**S 5.2**	**S 5.3**	**S 5.4**	**S 5.5**	**S 5.6**	**S 5.7**	**S 5.8**
Travel speed (mm/min)	75	85	95	105	115	125	135	150
Energy input (kJ/mm)	2.576	2.273	2.034	1.840	1.680	1.546	1.431	1.288
Scenario Num. for 125 Amps	**S 6.1**	**S 6.2**	**S 6.3**	**S 6.4**	**S 6.5**	**S 6.6**	**S 6.7**	**S 6.8**
Travel speed (mm/min)	75	85	95	105	115	125	135	150
Energy input (kJ/mm)	2.800	2.471	2.211	2.000	1.826	1.680	1.556	1.400

*S for Simulation …

Table 2. Reduction factors for stress-strain relationship of steel at elevated temperatures [39]

Steel temperature θ_a	Reduction factors at temperature relative to the value at 20°C		
	Effective yield strength	Proportional limit	Slope of the linear elastic range
	$k_{y,\theta} = f_{y,\theta} / f_y$	$k_{p,\theta} = f_{p,\theta} / f_y$	$k_{E,\theta} = E_{a,\theta} / E_a$
20	1,000	1,0000	1,0000
100	1,000	1,0000	1,0000
200	1,000	0,8070	0,9000
300	1,000	0,6130	0,8000
400	1,000	0,4200	0,7000
500	0,780	0,3600	0,6000
600	0,470	0,1800	0,3100
700	0,230	0,0750	0,1300
800	0,110	0,0500	0,0900
900	0,060	0,0375	0,0675
1000	0,040	0,0250	0,0450
1100	0,020	0,0125	0,0225
1200	0,000	0,0000	0,0000

Note: For intermediate values of the steel temperature, linear interpolation may be used

As evident from **Table 2**, an increase in temperature within a cross-section corresponds to a decrease in its yield strength. Consequently, this study employs a cross-sectional analysis approach that involves dividing the section into multiple groups. The first group encompasses the area with a yield strength of fy = 0. Subsequently, the remaining cross-section is subdivided into several pieces categorized by yield strength values that are in close proximity. This area segmentation aims to determine the cross-sectional area (A), which will subsequently influence the radius of gyration calculation and, consequently, the member's slenderness. As illustrated in **Figure 3**, the area division is facilitated by analysis software.

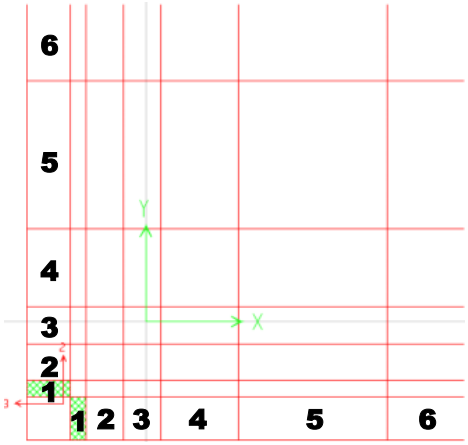

Parameter	Segment					
	1	2	3	4	5	6
A	1.45	3.35	3.42	7.07	13.54	6.96
J	0.86	6.81	7.12	26.57	63.96	25.95
I33	3.80	26.00	66.49	357.47	2095.18	2090.30
I22	3.80	26.00	66.49	357.47	2095.18	2090.30
I23	2.71	22.18	62.52	337.86	1981.46	2071.44
AS2	0.95	3.35	3.42	7.07	13.54	6.96
AS3	0.95	3.35	3.42	7.07	13.54	6.96
S33(+face)	1.81	6.11	11.09	34.15	110.83	100.74
S33(-face)	1.13	5.69	10.60	40.11	148.65	108.59
S22(+face)	1.13	5.69	10.60	40.11	148.65	108.59
S22(-face)	1.81	6.11	11.09	34.15	110.83	100.74
Z33	1.28	5.55	9.41	31.45	105.43	77.28

Figure 3. Segmen per segment section properties analysis

Each segmented region is assigned an area and a moment of inertia. Consequently, each segment possesses its own unique radius of gyration. The analysis proceeds by evaluating each modeled segment to determine its reduced compressive capacity. Subsequently, the total reduced compressive capacity for the entire cross-section is obtained by summing the contributions from all segments. This process is repeated for each welding simulation.

3. RESULTS AND DISCUSSION

Compressive strength due to welding speed variation

Figure 4 illustrates the load-carrying capacity of L 40.40.4 profiles under compressive force for various member lengths, ranging from 0.5 m to the slenderness limit defined as kL/r > 200. The figure also depicts the effects of different welding simulations on this capacity. The curve labeled "40.40.4 1.1 Ambient" represents the baseline compressive capacity of the 40.40.4 member at room temperature. The curves labeled "40.40.4 1.1 Heated" to "40.40.4 1.8 Heated" represent the reduced compressive capacity remaining in the 40.40.4 cross-section after welding simulations 1.1 to 1.8, respectively. The vertical separation between each "Heated" capacity curve and the "Ambient" curve quantifies the loss of compressive capacity attributable to the welding simulation. As evident from the figure, longer welded members exhibit a smaller decrease in their compressive capacity compared to shorter members.

Figures 5 and **Figure 6** depict analogous patterns for the 50.50.5 and 60.60.6 profile members, respectively. The analysis encompassed these member sizes, ranging from a length of 0.5 m to the threshold before slenderness classification (kL/r > 200). While the trends are generally similar, there are subtle variations in the compressive capacity reduction patterns. Notably, the 60.60.6 profile exhibits the least decrease in compressive capacity. Furthermore, compared to the 40.40.4 and 50.50.5 profiles, the 60.60.6 member demonstrates a steeper decline in compressive capacity during welding simulations compared to the thinner members (4 mm and 5 mm).

The observed lower reduction in compressive capacity for the 60.60.6 profile member compared to the thinner sections (4 mm and 5 mm) can be attributed to two key factors. Firstly, thicker steel sections generally experience a smaller heat-affected zone (HAZ) during welding. Secondly, the member length also plays a role in influencing the remaining compressive capacity. For a given current and voltage combination, the greatest loss of compressive capacity is likely to occur when the member length falls within the elastic-inelastic transition zone.

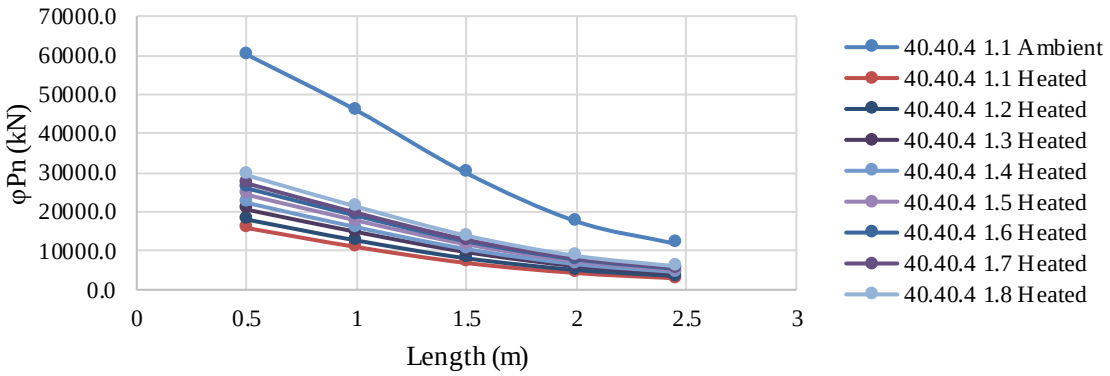

Figure 4. Compressive load carrying capacity for each simulation to each length of 40.40.4 member

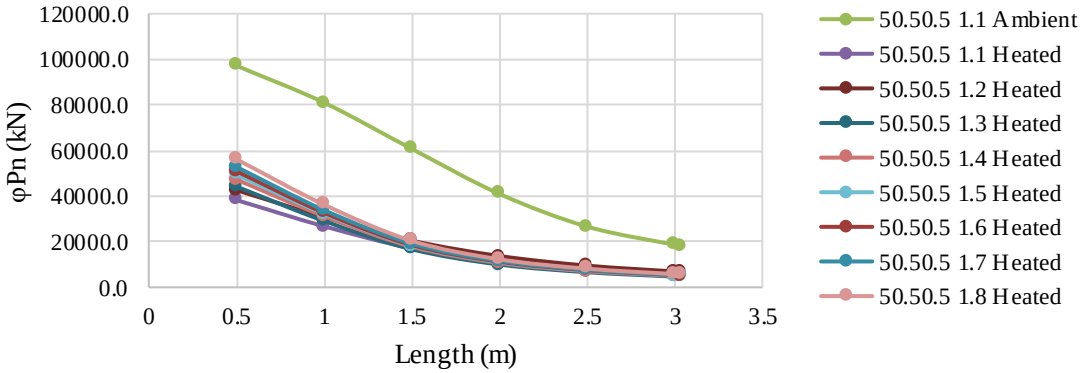

Figure 5. Compressive load carrying capacity for each simulation to each length of 50.50.5 member

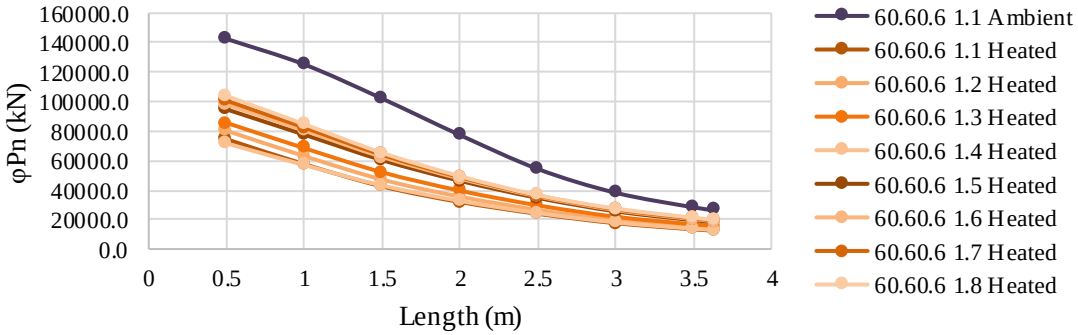

Figure 6. Compressive load carrying capacity for each simulation to each length of 60.60.6 member

Compressive strength due to current and welding speed variation

Building upon the previous simulations, this analysis extends the investigation to members with cross-sectional dimensions of 40.40.4, 50.50.5, and 60.60.6, as detailed in **Table 2**. Consistent with the trends observed in **Figure 7**, **Figure 8**, and **Figure 9** (illustrating the decrease in compressive capacity for 40.40.4, 50.50.5, and 60.60.6 cross-sections under simulation 1.i, respectively), the largest remaining compressive capacity is associated with welding simulation i.8 (fastest travel speed), while the smallest capacity is observed for simulation i.1 (slowest travel speed). Consequently, **Figure 10**, **Figure 11**, and **Figure 12** present the results for members 40.40.4, 50.50.5, and 60.60.6, respectively, under welding simulations i.1 and i.8 for further examination.

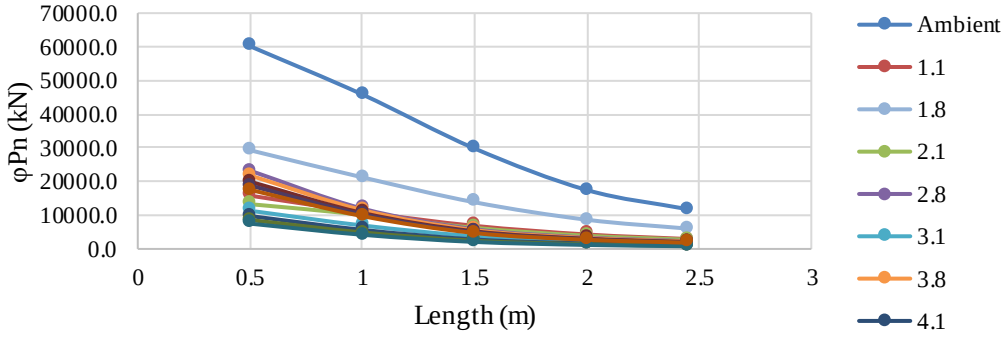

Figure 7. Resumed compressive load carrying capacity for each simulation to each length of 40.40.4 member

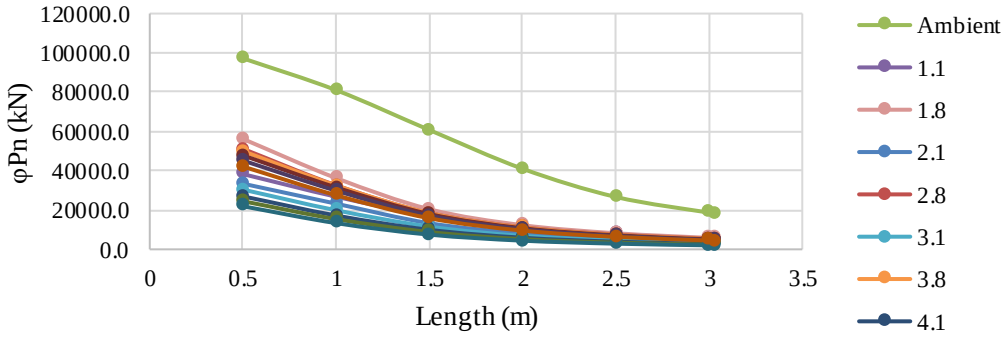

Figure 8. Resumed compressive load carrying capacity for each simulation to each length of 50.50.5 member

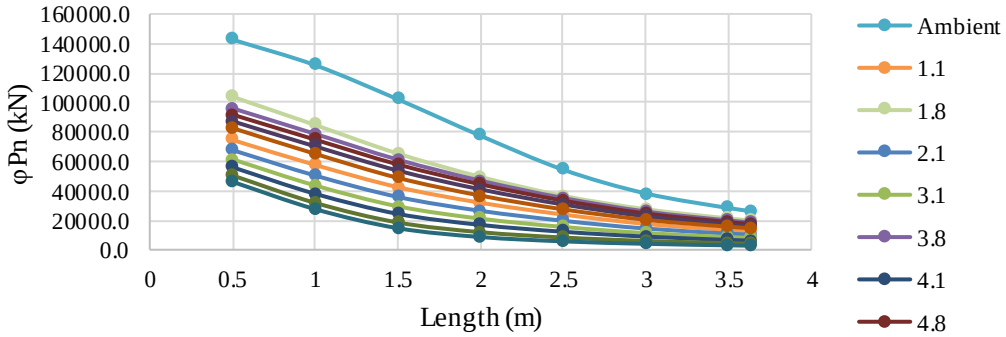

Figure 9. Resumed compressive load carrying capacity for each simulation to each length of 60.60.6 member

The findings from the simulations conducted on the 40.40.4, 50.50.5, and 60.60.6 cross-sections consistently demonstrate a pattern across all three thicknesses (4 mm, 5 mm, and 6 mm). For each cross-section, the highest remaining compressive capacity is observed under welding simulation i.8 (fastest travel speed), while the lowest remaining capacity occurs under simulation i.1 (slowest travel speed).

An analysis of the remaining compressive capacity for the 40.40.4 (**Table 3**), 50.50.5 (**Table 4**), and 60.60.6 (**Table 5**) cross-sections, as they vary with member length, reveals a consistent trend. As evident from the tables, welding parameters that combine lower current and higher travel speed lead to the highest remaining compressive capacity within the cross-section. Conversely, higher current and lower travel speed combinations result in the lowest remaining capacity. This observation can be attributed to the influence of net heat input (Hnet) on the heat-affected zone (HAZ) width. Hnet, in turn, is a function of welding current, power, speed, and thermal efficiency. While not a linear relationship, the width of the HAZ exhibits a positive correlation with the heat input experienced during welding.

Table 3. Remaining capacity of heated 40.40.4 section frame

Length (m)	φPn (kN) ambient	φPn' (kN) S 1.8	φPn' (kN) S 6.1	Remaining capacity for S 1.8*	Remaining capacity for S 6.1**
0.50	60185.9	29307.22	7511.359	48.69%	12.48%
1.00	45864.3	21260.04	4209.597	46.35%	9.18%
1.50	29818.8	13849.79	2078.121	46.45%	6.97%
2.00	17491.8	8666.521	1190.816	49.55%	6.81%
2.45	11785.0	6028.342	800.4505	51.15%	6.79%

Table 4. Remaining capacity of heated 50.50.5 section frame

Length (m)	φPn (kN) ambient	φPn' (kN) S 1.8	φPn' (kN) S 6.1	Remaining capacity for S 1.8*	Remaining capacity for S 6.1**
0.50	97200.1	56175.11	21916.31	57.79%	22.55%
1.00	80999.2	36256.72	13327.09	44.76%	16.45%
1.50	60732.3	20410.87	7486.354	33.61%	12.33%
2.00	40990.2	12294.63	4406.042	29.99%	10.75%
2.50	26650.7	8192.961	2885.043	30.74%	10.83%
3.00	18688.8	5836.679	2031.405	31.23%	10.87%
3.04	18270.1	5710.893	1986.315	31.26%	10.87%

Table 5. Remaining capacity of heated 60.60.6 section frame

Length (m)	φPn (kN) ambient	φPn' (kN) S 1.8	φPn' (kN) S 6.1	Remaining capacity for S 1.8*	Remaining capacity for S 6.1**
0.50	142584.1	103834.10	46094.94	72.82%	32.33%
1.00	125230.7	84642.16	27547.33	67.59%	22.00%
1.50	102052.2	65253.29	14624.00	63.94%	14.33%
2.00	77320.7	49412.93	8632.31	63.91%	11.16%
2.50	54297.9	36556.21	5680.00	67.33%	10.46%
3.00	38173.7	27462.12	4011.62	71.94%	10.51%
3.50	28284.2	21224.03	2979.61	75.04%	10.53%
3.64	26270.0	19906.18	2768.68	75.78%	10.54%

*) S 1.8 employed a travel speed of 2.50 mm/s, and 75 amps current
**) S 6.1 employed a travel speed of 1.25 mm/s, and 125 amps current

The most significant reduction in compressive capacity is observed when the member length falls within the elastic-inelastic buckling transition zone. This phenomenon occurs once the proportional limit is exceeded. As the member length increases and its behavior becomes more elastic, the magnitude of compressive capacity loss diminishes.

Temperature Distribution Along the Section

The observed decrease in yield strength and elastic modulus at elevated temperatures can be attributed to the weakening of interatomic bonds within the steel's microstructure. This phenomenon arises as temperature increases, causing thermal energy to vibrate the atoms in the steel lattice. These vibrations disrupt the orderly atomic arrangement, weakening the forces that hold the atoms together [40].

Yield strength signifies the stress level at which the steel transitions from elastic to plastic deformation. A decrease in yield strength due to elevated temperatures implies a lower load threshold for plastic deformation within the member. This consequence diminishes the member's load-carrying capacity and can lead to premature failure under compressive loading. Elastic modulus, on the other hand, reflects the steel's stiffness, essentially its resistance to elastic deformation. A lower elastic modulus translates to increased deflection under a given load. In compression members, this translates to greater bowing and potential buckling at a reduced critical load.

Simulation 1.8, characterized by the lowest current variation and highest travel speed, represents the scenario with minimal compressive capacity loss. Conversely, simulation 6.1, employing the highest current variation and lowest travel speed, exemplifies the conditions that lead to the most significant reduction in compressive capacity. In essence, these simulations establish the upper and lower bounds for the compressive capacity loss observed in the steel members.

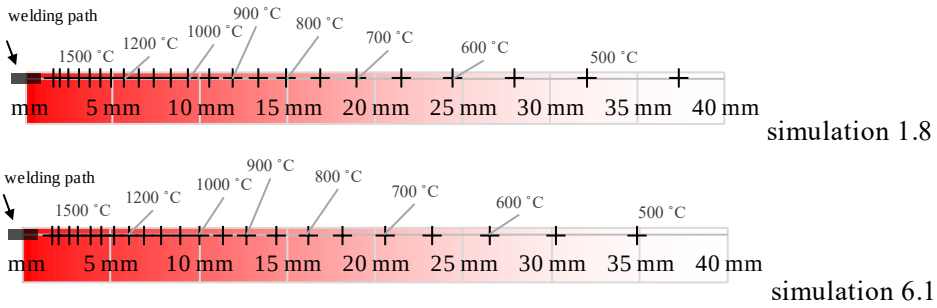

Figure 10. Comparison of 4 mm thick cross-sections welded with simulations 1.8 and 6.1

Figure 10 illustrates that upon contact with the 4 mm thick steel cross-section, the tip of the profile flange retains a temperature exceeding 450°C. Furthermore, the temperature at the edge of the cross-section welded using simulation 1.8 remains below 450°C, whereas the edge welded with simulation 6.1 surpasses this temperature. These observations suggest that when welding the 40.40.4 member, the entire weld path experiences temperatures exceeding 450°C, eliminating any region within the cross-section that retains its base metal behavior. In other words, the entire cross-section transforms into the heat-affected zone (HAZ).

Notably, the 5 mm plate welded with simulation 1.8 exhibits a section of base metal exceeding 20 mm along its length due to a cross-section temperature remaining below 200°C. Conversely, the edge of the 5 mm plate welded with simulation 6.1 retains a temperature between 300°C and 350°C. This observation suggests that when welding the 5 mm thick cross-section using simulation 6.1, the entire cross-section transforms into the heat-affected zone (HAZ).

The 6 mm plate welded with simulation 1.8 retains a substantial section of base metal exceeding 35 mm in length due to a cross-section temperature that remains below 200°C. In contrast, the edge of the 6 mm plate welded with simulation 6.1 exhibits a temperature of approximately 250°C. While the entire cross-section transforms into the heat-affected zone (HAZ) when welding the 6 mm section using simulation 6.1, the reduction in capacity at this temperature is likely to be comparatively minimal.

4. CONCLUSIONS

Higher welding currents demonstrably lead to a more extensive distribution of elevated temperatures within the cross-section. This directly translates to a reduction in both yield strength and elastic modulus. The magnitude of this reduction is directly proportional to the increase in temperature experienced by the cross-section. In simpler terms, higher welding currents induce a more pronounced decrease in yield strength and elastic modulus.

Welding speed demonstrably influences the remaining compressive capacity, with higher speeds resulting in a more favorable outcome. The observed trends in remaining compressive capacity, for each member length variation, exhibit a similarity to the behavior of members at room temperature. However, this similarity diminishes with increasing member length. In other words, the gap between the trends observed for room temperature and welding conditions narrows as the welded member length grows.

The study reveals that the most favorable scenario for minimizing compressive capacity loss is achieved by employing the highest welding speed and the lowest current setting. For instance, with a welding current of 75 amps, 35 volts, and a travel speed of 150 mm/min, the remaining compressive capacity for the 40.40.4, 50.50.5, and 60.60.6 cross-sections is measured at 51.15%, 57.79%, and 75.78%, respectively. Conversely, a worst-case scenario employing a current of 125 amps, 35 volts, and a travel speed of 75 mm/min would significantly reduce the remaining capacity to a mere 6.79% for the 40.40.4 member, 10.87% for the 50.50.5 member, and 10.54% for the 60.60.6 member. It is noteworthy that the decrease in compressive capacity observed across all cross-sections generally diminishes with increasing member length.

The simulation results demonstrate a clear correlation between welding parameters and compressive capacity loss. Specifically, employing the lowest welding speed and highest current demonstrably leads to the greatest reduction in compressive capacity. This phenomenon can be directly attributed to the resulting temperature distribution within the member's cross-section. Welding at these settings induces a scenario where the entire cross-section falls within the heat-affected zone (HAZ), effectively eliminating any remaining base metal that retains its original properties.

5. REFERENCES

[1] W.S. Alaloul, M. Altaf, M.A. Musarat, M.

Faisal Javed, A. Mosavi. 2021. *Systematic Review of Life Cycle Assessment and Life Cycle Cost Analysis for Pavement and a Case Study*. Sustainability 2021, 13, 4377. dx.doi.org/10.20944/preprints202103.0316.v1

[2] Robert Osei-Kyei, Vivian Tam, Mingxue Ma, Fidelis Mashiri. 2021. *Critical review of the threats affecting the building of critical infrastructure resilience.* International Journal of Disaster Risk Reduction, Volume 60. 102316, ISSN 2212-4209, https://doi.org/10.1016/j.ijdrr.2021.102316

[3] Sarah Bell, Charlotte Johnson, Kat Austen, Gemma Moore, Tse-Hui Teh. 2023. *Co-designing Infrastructures*. ISBN: 9781800082229. UCL Press. http://dx.doi.org/10.14324/111.9781800082229

[4] R. Kazancıoğlu, Özcan Erdoğan. 2023. *Resilience of hospital in disaster*. Journal of Design for Resilience in Architecture and Planning, 4 (Special Issue), 141–151. https://doi.org/10.47818/DRArch.2023.v4si115

[5] Charles G. Salmon, John E. Johnson, Faris A. Malhas. 2008. *Steel Structures: Design and Behavior (5th Edition)*. Prentice Hall

[6] Welding Research Council. 2005. Welding Research Council Bulletin: *Welding of Steel Structures for Seismic Resistance* (https://www.aws.org/)

[7] D.K. Dwivedi. 2022. *Arc Welding Processes: Shielded Metal Arc Welding: Welding Current and Metal Transfer*. In: "Fundamentals of Metal Joining". Springer, Singapore. https://doi.org/10.1007/978-981-16-4819-9_12

[8] American Institute of Steel Construction. (2017). *Modern Steel Construction Manual.* AISC

[9] D. Wang, Weihong Zhang, J. Jiang. 2002. *Combined shape and sizing optimization of truss structures*. Computational Mechanics. 29. 307-312. http://dx.doi.org/10.1007/s00466-002-0343-x

[10] Mehdi Jalalpour, Takeru Igusa, James K. Guest. 2011. *Optimal design of trusses with geometric imperfections: Accounting for global instability*. International Journal of Solids and Structures, Volume 48, Issue 21, Pages 3011-3019, ISSN 0020-7683, https://doi.org/10.1016/j.ijsolstr.2011.06.020.

[11] Limin Lu, Guanglin Yuan, Zhaohui Huang, Qianjin Shu, Qing Li. 2017. *Performance-based analysis of large steel truss roof structure in fire*. Fire Safety Journal, Volume 93, Pages 21-38, ISSN 0379-7112, https://doi.org/10.1016/j.firesaf.2017.08.002.

[12] R.H. Leggatt. 2008. *Residual stresses in welded structures*. International Journal of Pressure Vessels and Piping. 85. 144-151. http://dx.doi.org/10.1016/j.ijpvp.2007.10.004

[13] Malik Mushthofa, Fakhri Pratama Nurfauzi, Astriana Hardawati. 2023. *Investigation of effective section reduction in low carbon steel during SMAW welding*. Teknisia 28(2):79-89 http://dx.doi.org/10.20885/teknisia.vol28.iss2.art2

[14] John C. Lippold. 2014. *Welding Metallurgy and Weldability*. ISBN:9781118230701. John Wiley & Sons, Inc. DOI:10.1002/9781118960332

[15] J. Zhou, H.L. Tsai. 2005. *Welding heat transfer*. Woodhead Publishing Series in Welding and Other Joining Technologies, Processes and Mechanisms of Welding Residual Stress and Distortion. Woodhead Publishing, Pages 32-98, ISBN 9781855737716, https://doi.org/10.1533/9781845690939.1.32.

[16] Chai H Yoo, Sung Lee. 2011. *Stability of Structures Principles and Applications*. ISBN: 9780123851222. Butterworth-Heinemann

[17] Luca Possidente, Nicola Tondini, Jean-Marc Battini. 2021. *Numerical analysis of the torsional and flexural-torsional buckling behaviour of compressed steel members at elevated temperature*. ce/papers (Proceedings in civil engineering) 4. 1239-1245. http://dx.doi.org/10.1002/cepa.1417

[18] Y. Zhang, G. Shi, Z. Liu, Y. Wang, Y. Shi. 2011. *Finite element analysis and design method study for the local buckling of high-strength steel equal angles under axial compression*. Tumu Gongcheng Xuebao/ China Civil Engineering Journal. 44. 27-34.

[19] Yueqi Bi, Xiaoming Yuan, Mingrui Hao, Shuai Wang, He Xue. 2022. *Numerical Investigation of the Influence of Ultimate-Strength Heterogeneity on Crack Propagation and Fracture Toughness in Welded Joints*. Materials. 15. 3814. 10.3390/ma15113814.

[20] Zhuyao Zhang, Steve Roberts, Josh Wildgoose, Will Philpott, Mark Jepson. 2024. *Effects of post-weld heat treatment on the microstructure and properties of the matching SMAW filler metal for weld joints in MarBN*

steel. Welding in the World. 10.1007/s40194-023-01653-w.

[21] Huan Qi, Pang Qihang, Weijuan Li, and Shouyuan Bian. 2024. *The Influence of the Second Phase on the Microstructure Evolution of the Welding Heat-Affected Zone of Q690 Steel with High Heat Input*. Materials. 17. No. 3: 613. https://doi.org/10.3390/ma17030613

[22] Yue Zhang, Jun Xiao, Wei Liu, and Aimin Zhao. 2021. *Effect of Welding Peak Temperature on Microstructure and Impact Toughness of Heat-Affected Zone of Q690 High Strength Bridge Steel*. Materials .14. No. 11: 2981. https://doi.org/10.3390/ma14112981

[23] Klas Weman. 2003. "Welding processes handbook Second Edition". Woodhead Pub. ISBN 978-0-85709-518-3

[24] C.H. Yoo, & S. Lee. 2011. *Stability of Structures: Principles and Applications.* Butterworth-Heinemann. Elsevier. ISBN: 978-0-12-385122-2 http://dx.doi.org/10.1016/C2010-0-66075-5

[25] Lingyu Zhou, Liqiang Jiang, Liping Wang. 2022. *Design of Steel Structures: Materials, Connections, and Components*. ISBN 978-0-323-91682-0. Published by Elsevier. https://doi.org/10.1016/C2021-0-00344-8

[26] Leroy Lutz. 2006. *Evaluating single-angle compression struts using an effective slenderness approach*. Engineering Journal (New York). 43. 241-246.

[27] William T. Segui. 2006. *Steel Design 5th*. ISBN-13: 978-1-111-57600-4. Cengage Learning

[28] Yordan Denev. (2022). *Analyze of Welding Arc Parameters In Shielded Metal Arc Welding*. International Scientific Journal "Machines. Technologies. Materials". Year xvii, issue 2, p.p. 80-82 (2023) http://dx.doi.org/10.5281/zenodo.6884587.

[29] American Society of Mechanical Engineers (ASME) Section IX. 2021. *The qualification standard for welding and brazing procedures*.

[30] British Standard BS EN 1011-1. 2009. *Welding — Recommendations for welding of metallic materials*.

[31] Rudra Singh, R.C. Gupta, S. Sarkar. 2013. *Analysis of Depth of Penetration and Bead Width of Shielded Metal Arc Weld under Magnetic Field Applying Artificial Neural Networks*. International Journal of Science, Engineering and Technology Research (IJSETR) Volume 2, Issue 2, February 2013 10.13140/RG.2.2.25076.14722.

[32] D.S. Nagesh, G.L. Datta. 2002. *Prediction of weld bead geometry and prediction in shielded metal-arc welding using artificial neural networks*. Journal of Materials Processing Technology. 123. 303–312. 10.1016/S0924-0136(02)00101-2.

[33] Sudhir Kumar, Rajender Singh. 2019. *Investigation of tensile properties of shielded metal arc weldments of AISI 1018 mild steel with preheating process*. Materials Today: Proceedings. 26. http://dx.doi.org/10.1016/j.matpr.2019.10.167

[34] Ashok Tadamalle, Y. Reddy. 2020. *Fatigue Life Prediction of Dissimilar Metal Laser Weld Joints*. Journal of The Institution of Engineers (India): Series C. 101. http://dx.doi.org/10.1007/s40032-020-00603-5

[35] Michael Bassey, Jephtar Ohwoekevwo, Aniekan Ikpe. 2024. *Thermal analysis of AISI 1020 low carbon steel plate agglutinated by gas tungsten arc welding technique: a computational study of weld dilution using finite element method*. Journal of Engineering and Applied Science. 71. 1-22. 10.1186/s44147-024-00375-0.

[36] Anthony Murphy, John Lowke. 2017. *Handbook of Thermal Science and Engineering*. ISBN : 978-3-319-32003-8. Springer. http://dx.doi.org/10.1007/978-3-319-26695-4_29.

[37] Zong Ran, J. Chen, C.S. Wu, Girish Padhy. 2016. *Influence of shielding gas on undercutting formation in gas metal arc welding*. Journal of Materials Processing Technology. 234. 169-176. 10.1016/j.jmatprotec.2016.03.020.

[38] Paul Kah, Hamidreza Latifi, Raimo Suoranta, Jukka Martikainen, Markku Pirinen,. 2014. *Usability of arc types in industrial welding*. International Journal of Mechanical and Materials Engineering. 9. 1-12. 10.1186/s40712-014-0015-6.

[39] Wei Lu, Pentti Mäkeläinen, Painopörssi. 2003. "Advanced Steel Structures - Fire and Fatigue Design". Helsinki University of Technology.

[40] Mina Seif, Joseph Main, Jonathan Weigand, Fahim Sadek, Lisa Choe, Chao Zhang, John Gross, William Luecke, David McColskey.

2016. *Temperature-Dependent Material Modeling for Structural Steels: Formulation and Application*. NIST Technical Series Publications.